Acta Cryst. (1998). A**54**, 306–319

Structure Model for the Phase Al_mFe Derived from Three-Dimensional Electron Diffraction Intensity Data Collected by a Precession Technique. Comparison with Convergent-Beam Diffraction

J. GJØNNES,[a]* V. HANSEN,[a] B. S. BERG,[a]† P. RUNDE,[a] Y. F. CHENG,[b]‡ K. GJØNNES,[a]§ D. L. DORSET[c] AND C. J. GILMORE[d]

[a]*Centre for Materials Science, University of Oslo, Gaustadalléen 21, 0371 Oslo, Norway,* [b]*Max-Planck-Institut für Metallforschung, Seestrasse 92, 70174 Stuttgart, Germany,* [c]*Hauptmann–Woodward Medical Research Institute, Buffalo, NY 14203-1196, USA, and* [d]*Department of Chemistry, University of Glasgow, Glasgow G12 8QQ, Scotland. E-mail: jon.gjonnes@fys.uio.no*

(*Received 8 September 1997; accepted 17 November 1997*)

Abstract

Three-dimensional electron diffraction intensity data have been collected for the metastable alloy phase Al_mFe by a precession technique. The structure model has been derived by Patterson and Fourier calculations and by the direct method using either maximum entropy and likelihood or the tangent formula; both were based on the kinematical scattering approximation. Energy-filtered convergent-beam profiles for reflections along two systematic rows *h*00 and *hh*0 were used to determine the corresponding structure factors; these were introduced in a dynamical scattering correction procedure for all *hk*0 structure factors. The tetragonal Al_mFe structure ($a = 8.84$, $c = 21.6$ Å, space group $I\bar{4}2m$) with 90 Al and 20 Fe atoms can be described by ten-coordinated Fe or by a distorted CsCl-type network with vacancies.

1. Introduction

Aluminium alloys contain a variety of stable and metastable Al–Fe–Si intermetallic phases as primary particles, secondary particles and precipitates. For many of the phases, the crystal structure is unknown, mainly due to lack of single crystals suitable for X-rays. This can be a problem even for stable phases: owing to extensive faults, the crystal structure of the commonly occurring alloy phase β-$Al_{4.5}FeSi$ could be determined only by a combined electron diffraction and single-crystal X-ray effort (Rømming *et al.*, 1994). For metastable phases like Al_mFe, which occur as μm-size particles in an aluminium matrix, usually together with other intermetallic phases, electron diffraction appears as the only viable alternative for crystal structure determination.

Al_mFe was first reported by Miki *et al.* (1975) and is commonly found as primary particles in aluminium alloys cast in industrial processes at high cooling rates. Lattice parameters of the body-centred tetragonal unit cell are $a = 8.84$, $c = 21.6$ Å, $m = 4.2$–4.4 (Westengen, 1982). An attempt to derive a crystal structure was made by Skjerpe (1988). From qualitative considerations of electron diffraction patterns and high-resolution images, he suggested a tentative model with 20 Fe and 90 Al atoms in the space group $I4/mmm$, which was proposed from convergent-beam patterns. He also reported extensive faults in the crystals, especially on (110) planes. However, with a unit-cell content of approximately 110 atoms and no short axis, a structure solution must be based on three-dimensional intensity data, which had to be collected from several precipitate crystals of moderate thickness. In electron diffraction, such data are expected to be strongly influenced by dynamical scattering effects. No well established procedure existed that could be applied directly to this kind of problem. We have therefore explored different electron diffraction techniques: selected-area (SAD) spot patterns; precession patterns (Vincent & Midgley, 1994); unfiltered and energy-filtered CBED patterns; and applied different calculation schemes for the structure solution. The main structure result was derived by adapting traditional crystallographic methods within the kinematical approximation. Dynamical calculations applied to CBED measurements (Cheng *et al.*, 1996) served as a confirmation and were also used to improve some of the experimental data by a procedure described by Gjønnes *et al.* (1998). The resulting structure solution is discussed in relation to other phases in the aluminium–iron system.

Electron crystallographic techniques have recently been applied succesfully to several organic and inorganic structures: by a combination of high-resolution images and diffraction intensities (*e.g.* Weirich *et al.*, 1996; Andersen *et al.*, 1998; Zou *et al.*, 1993) or by treating diffracted intensities by mathematical procedures taken from X-ray crystallography, see *e.g.* Dorset (1995). The present work differs somewhat from these

† Present address: Hydro Aluminium R&D Materials Technology, 4265 Håvik, Norway.

‡ Present address: International Institute for Advanced Research, Central Research Laboratories, Matsushita Electrical Industries Co. Ltd, 3-4 Hikaridai, Seika, Kyoto 619-02, Japan.

§ Present address: National Institute for Occupational Health, PO Box 8149 Dep, 0033 Oslo, Norway.

studies by being based on crystals of irregular shape and moderate thickness, which is expected to exacerbate the problems associated with dynamical scattering.

2. Material

Material for the study was obtained from a commercial aluminium alloy AA5052, which had been produced by a pilot twin-roll caster at Hydro Aluminium as Karmøy. Al_mFe particles together with other primary particles present in the alloy were extracted by the butanol method described by Simensen *et al.* (1984). The particles were collected on a micropore filter and transferred to an electron-microscope grid with a holey carbon film, see Fig. 1. Spot patterns and some CBED patterns were obtained in JEOL 2000 FX and 200CX electron microscopes; the precession patterns were taken in a Philips EM430 at Bristol University, and the CBED profiles in a Zeiss EM912 omega energy-filter microscope at MPI, Stuttgart.

3. Electron diffraction

3.1. *Spot patterns and precession patterns*

Typical selected-area spot patterns are reproduced in Fig. 2. As a first attempt, three-dimensional electron diffraction intensity data were collected from a series of spot pattern photographs taken in a microdiffraction mode. Photometered intensities were combined into a data set that included 185 unique reflections inside $d = 1.3$ Å. Patterson projections and sections calculated from these data indicated that they did indeed contain information about the structure, see Figs. 3(*a*),(*b*). However, the precession technique invented by Vincent & Midgley (1994) seemed much better suited for acquiring three-dimensional intensities from such specimens. A new set of intensity data was therefore collected by the equipment at Bristol University.

The precession technique is in principle equivalent to the precession camera used in X-ray diffraction (see *e.g.* Buerger, 1964), except that the crystal is not precessed; a precession motion is instead applied synchronously to the incident electron beam above and to the diffraction pattern below the specimen. Such motions can be produced with the aid of the tilting coils which are standard in modern electron microscopes. The precession technique has some important advantages over the usual selected-area spot pattern: the intensity of each

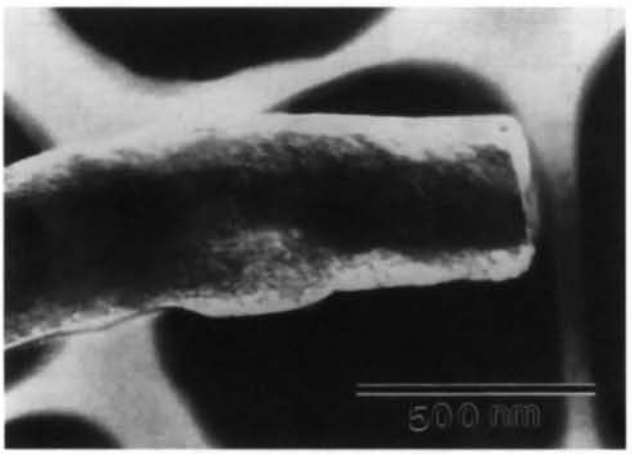

Fig. 1. Dark-field image of an extracted Al_mFe particle.

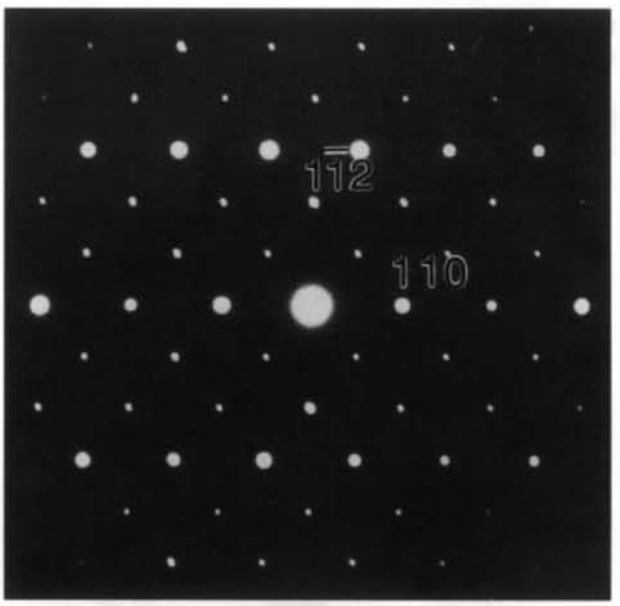

(*a*)

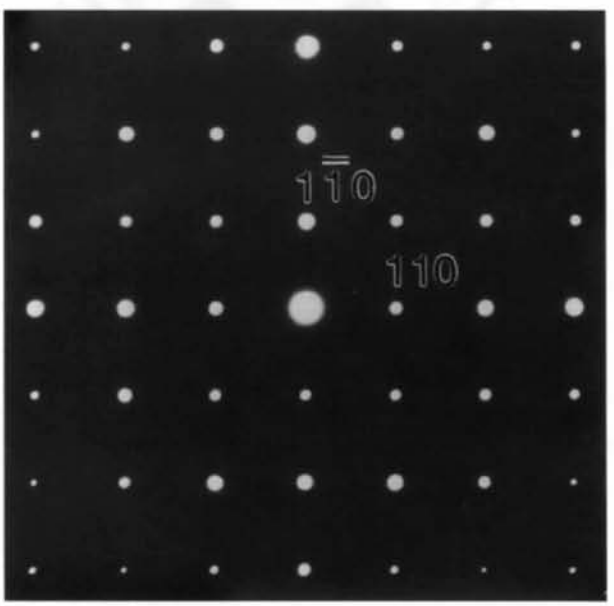

(*b*)

Fig. 2. Selected-area diffraction patterns taken as projections along (*a*) [111] and (*b*) [001].

reflection is the result of integration through the Bragg angle in much the same way as in single-crystal X-ray diffraction. Data will extend further out in the zone. Dynamical effects will be reduced by the tilt off the zone axis; see the schematic 'still' representation of the beam configuration in Fig. 4. Thickness oscillations in particular will be damped considerably by the integrating motion. As a consequence, we expect the precession intensity data to be more kinematic like than SAD spot intensities, especially when the crystal is not very thin. Dynamical scattering calculations will on the other hand be more complicated since the intensity will be a sum of contributions along the precession circle. It was decided to treat the intensity data as kinematical.

Precession patterns from eight different projections, [111], [001], [100], [110], [120], [140], [302], [301], two exposures from each, were recorded on film (Fig. 5).

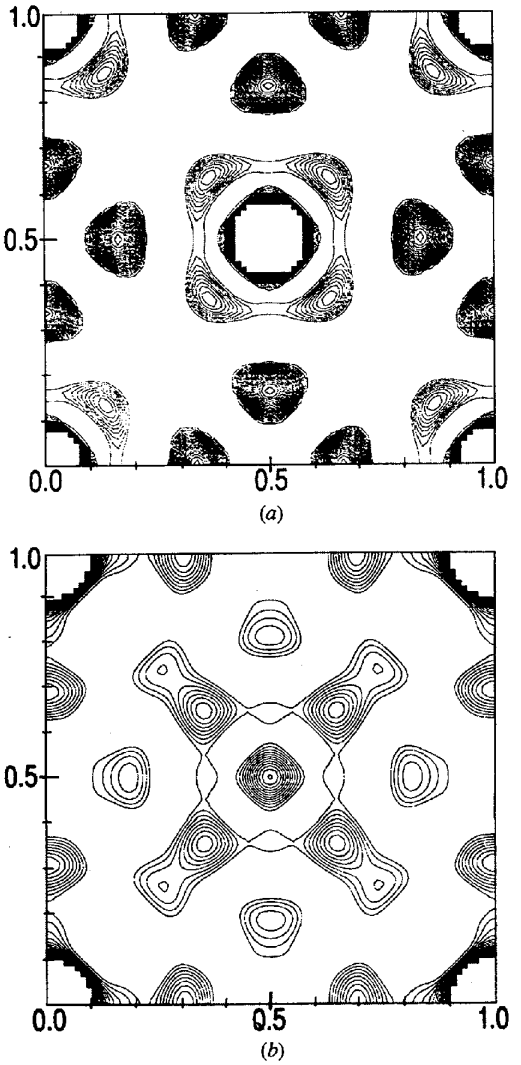

Fig. 3. Patterson maps calculated from spot pattern intensities. (*a*) [001] projection; (*b*) (u, v) section for $w = 0$.

The improvement in comparison with traditional spot patterns taken at a comparable thickness was apparent. The diffraction photographs were processed through several stages in order to produce a three-dimensional data set. The negatives were placed on a light box. The optical density was recorded by a CCD camera and transferred to an imaging analysis system (Kontron Vidas 25) in a 512 × 512 pixel size and converted to intensities with the aid of a grey-scale calibration curve obtained by a set of time exposures in the electron microscope. The intensities in rows of reflections were read along a line one pixel wide and integrated after subtraction of background. The whole procedure is described in detail elsewhere (Berg *et al.*, 1998). Equivalent reflections in the projection were averaged and a geometrical correction factor analogous to the Lorentz factor in X-ray diffraction was applied to the intensities (Vincent & Midgley, 1994), *viz*†

$$I_{\text{corr}} = I \sin\varepsilon \quad \text{where} \quad \cos\varepsilon = (g_n^2 - 2nkh)/2KG_n,$$

where g_n is the reciprocal-lattice vector in the Laue zone n: $g_n = g_0 + n_h$. h is the reciprocal-lattice spacing perpendicular to the zero layer and k is the wave number of the incident electron. K is the transverse component of k and is related to the precession angle φ by $K = k \tan\varphi$.

Reflections outside a sphere of radius corresponding to $d = 0.66$ Å and reflections in the second- and higher-

† During the course of this work, a slightly different correction factor was derived by one of us (Gjønnes, 1997).

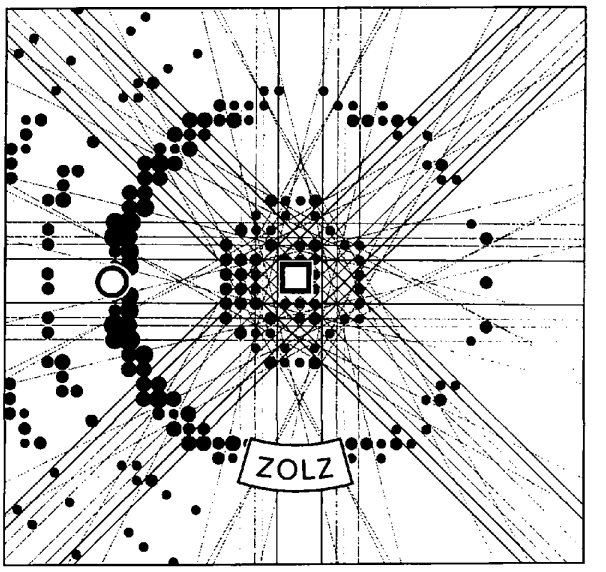

Fig. 4. Schematic representation of beams at one instant on the precession circle used in [001] projection. The position of the direct beam is marked by an open circle, the zone axis by a square. During the precession motion, the direct beam moves around the Laue circle (ZOLZ). (In an equivalent description, the Laue circle is rotated around the central beam.)

order Laue zones in the [001] projection were removed from the data. About 500 measured unique reflections were included in this procedure. Inside $d = 1$ Å, 285 of the reflections (95%) were recorded and supplemented with the remaining intensities from the spot patterns mentioned above.

3.2. *Merging to three-dimensional data*

Intensity data from the eight projections were merged into a single three-dimensional data set. This was achieved by means of the intensity ratios α_{mn} between different projections as obtained from common rows of reflections. By disregarding effects of dynamical scattering (especially non-systematic dynamical scattering), we could determine 28 such ratios:

$$\alpha_{mn} = (1/n) \sum_{g} \alpha^{g}_{mn}$$

from one to six reflections, g, in the common row. Scaling factors A_n for the eight projections were then calculated by a least-squares method. A linear procedure was found to be inadequate and a non-linear least-squares procedure based on the Levenberg–Marquard method (Press *et al.*, 1986) was adapted. This merger is seen as the most uncertain step in the present experiment. An estimate of the error in the intensities can be obtained from reflections that are included in several projections. From 13 reflections appearing in four projections, an average standard uncertainty of 36% in

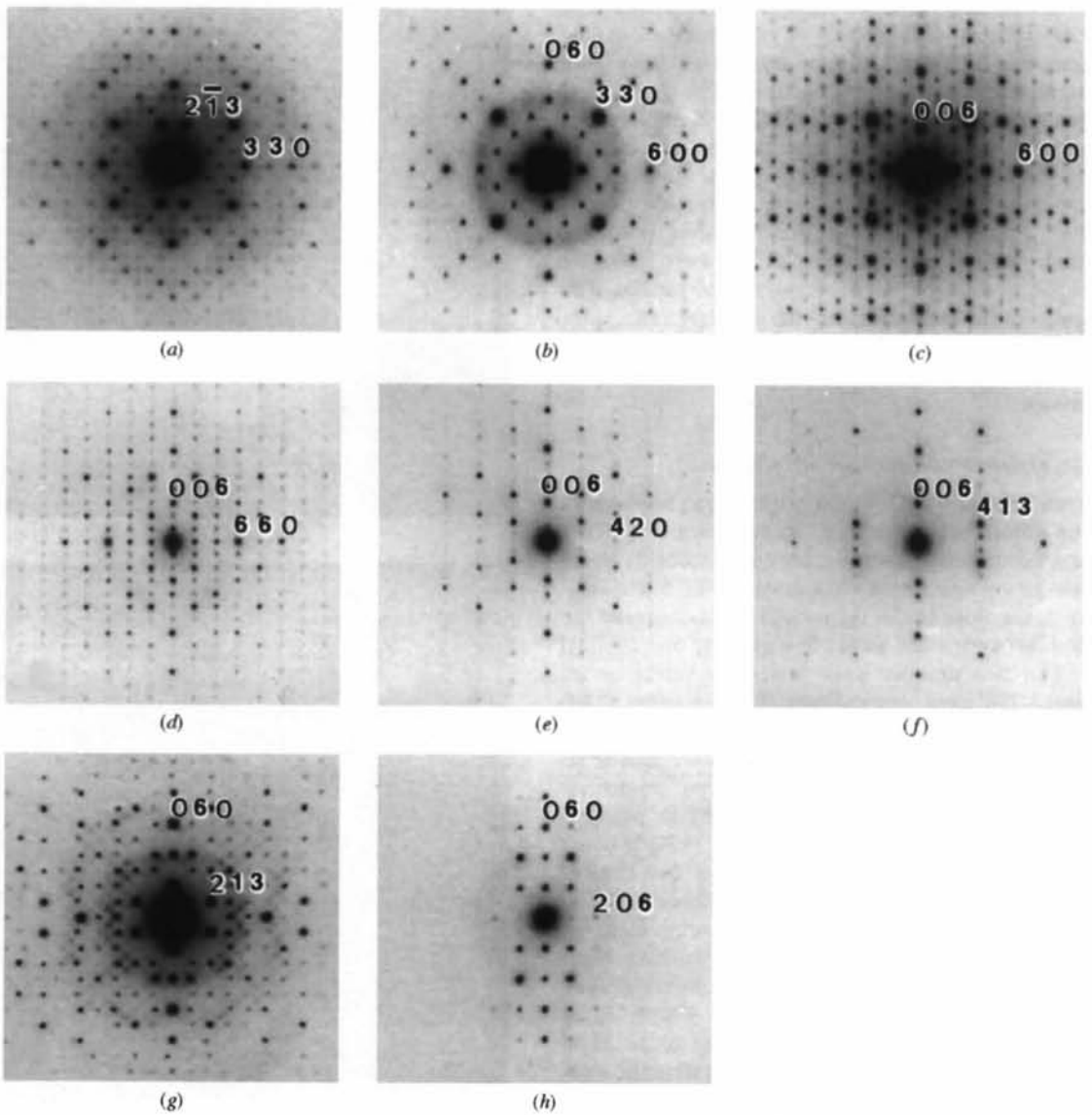

Fig. 5. Precession photographs taken in the eight projections (*a*) [11$\bar{1}$], (*b*) [001], (*c*) [010], (*d*) [1$\bar{1}$0], (*e*) [1$\bar{2}$0], (*f*) [1$\bar{4}$0], (*g*) [30$\bar{2}$], (*h*) [30$\bar{1}$], reproduced as printouts from the CCD camera. Modulations along the c^* axis are seen most clearly in [010] projection.

Table 1. *Absolute structure factors in* $\mathring{A}^{-2}$ *for h00 and hh0 reflections obtained from filtered CBED profiles*

*h*00 values taken from Cheng *et al.* (1996).

U_{200} = −0.01191 (31)	U_{110} = +0.00290 (45)
U_{400} = +0.01592 (44)	U_{220} = −0.00199 (23)
U_{600} = +0.01275 (16)	U_{330} = +0.03872 (9)
U_{800} = −0.00653 (72)	U_{440} = +0.00750 (34)
$U_{10,0,0}$ = +0.00359 (33)	U_{550} = +0.00773 (107)
$U_{12,0,0}$ = −0.00135 (18)	U_{660} = +0.00226 (51)
$U_{14,0,0}$ = −0.00214 (31)	U_{770} = +0.00158 (27)
	U_{880} = +0.00514 (40)
	U_{990} = +0.00300 (18)
	$U_{10,10,0}$ = +0.00140 (11)
	$U_{11,11,0}$ = +0.00210 (8)

the intensities was obtained. Non-systematic dynamical effects were considered to be a major source of error. In order to reduce this error, an alternative scaling procedure was adopted at a later stage. The dense [00*l*] was emphasized as a common row. The dynamical effects in a dense row are expected to be dominated by systematic interactions along the row and hence to be less dependent on the actual projection. Four of the eight projections could then be scaled directly by using the α_{mn}'s for which [00*l*] is the common row; the remaining projections were scaled to these four by using the α_{mn} with the lowest standard deviations. The average standard deviation for the same 13 reflections as above was then reduced to 27%. Both three-dimensional sets were used in the crystallographic calculations.

3.3. *Convergent-beam electron diffraction*

Several CBED-based techniques were applied in order to obtain supplementary information about the structure. Examples of patterns taken in order to check the space-group symmetry are shown in Fig. 6. Patterns with the beam close to the tetragonal axis confirmed the projected 4*m* symmetry, indicating at least one vertical mirror. The two mirrors were tested by tilting about [110] and [100] axes, respectively. The diagonal (110) mirror seemed well confirmed, whereas the (100) mirror appeared less certain, see below. Quantitative structure-factor information can be obtained from intensities integrated across high-order lines in CBED patterns (Taftø & Metzger, 1985; Gjønnes & Bøe, 1994; Vincent *et al.*, 1984) and especially from one- or two-dimensional intensity profiles in energy-filtered CBED patterns, which have been applied to refinement of parameters or structure factors in known structures with small unit cells, see *e.g.* Bird & Saunders (1992); Spence (1993); Tsuda & Tanaka (1995). Cheng *et al.* (1996) have extended the latter technique to *ab initio* determination of structure factors in a systematic row. From energy-filtered CBED intensity profiles of the *h*00, $h = 2$ to $h = 14$, structure-factor amplitudes and signs for Al_mFe were obtained by means of an iterative procedure based on dynamical scattering calculations. Details of the procedure are given by Cheng *et al.* (1996). At first, a two-beam-like profile was fitted to a strong reflection in the row; more profiles, beams and structure factors were gradually added in the calculations. The [001] projection is centrosymmetric (see below) and different sign combinations were tried during the process, which led to a unique answer. In the present work, this technique has been extended to include also *hh*0 ($h = 1$ to 11). The structure-factor results summarized in Table 1 were used to check the models derived from the precession data and in a late

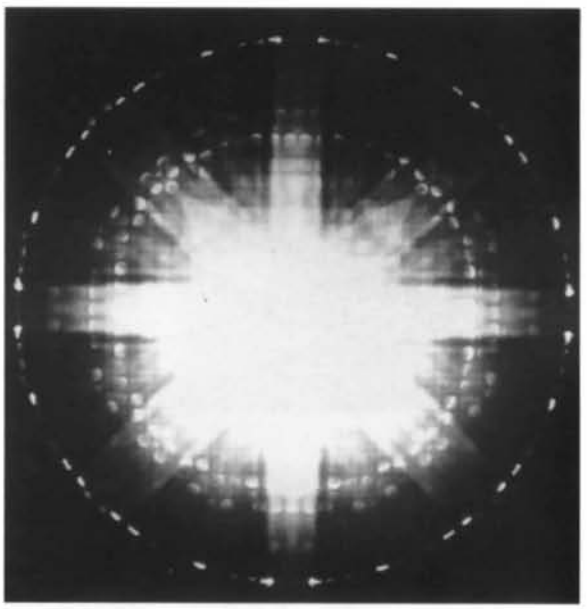

(*a*)

(*b*)

Fig. 6. CBED patterns (*a*) along [001] and (*b*) tilted around [110].

stage as input in a dynamical correction procedure developed by Gjønnes *et al.* (1998) for *hk*0 precession intensities.

4. Calculations and interpretations

4.1. *Patterson calculations and space-group assignment*

As a first step in the structure analysis, a series of Patterson maps were calculated from the three-dimensional intensity data as projections along the *a* and *c* axes and as *uv* sections at different heights *w*. Examples are shown in Fig. 7. The six most prominent peaks are listed in Table 2. The very strong peak at (0, 0, 0.30) is noted. The Patterson sections also revealed salient information concerning the space-group symmetry: the *uv*0 map (Fig. 7*b*) is not consistent with the 4*mm* three-dimensional symmetry that Skjerpe (1988) had assumed from CBED patterns (see also Skjerpe *et al.*, 1987). The strong peak at (0.37, 0.37, 0) fits well with the diagonal mirror. But there is no corresponding vector that would relate to the (100) mirror. From our CBED pattern, we were satisfied that 4*mm* projected symmetry must be correct, see above. There is no evidence of a screw axis; it was therefore concluded that the fourfold axis must

Table 2. *Strongest peaks in Patterson maps (zero peak is 100)*

	u	*v*	*w*	Height
1	0.50	0.50	0.20	50
2	0.37	0.00	0.15	28
3	0.50	0.50	0.10	24
4	0.37	0.37	0.00	23
5	0.50	0.13	0.05	14
6	0.37	0.37	0.30	14

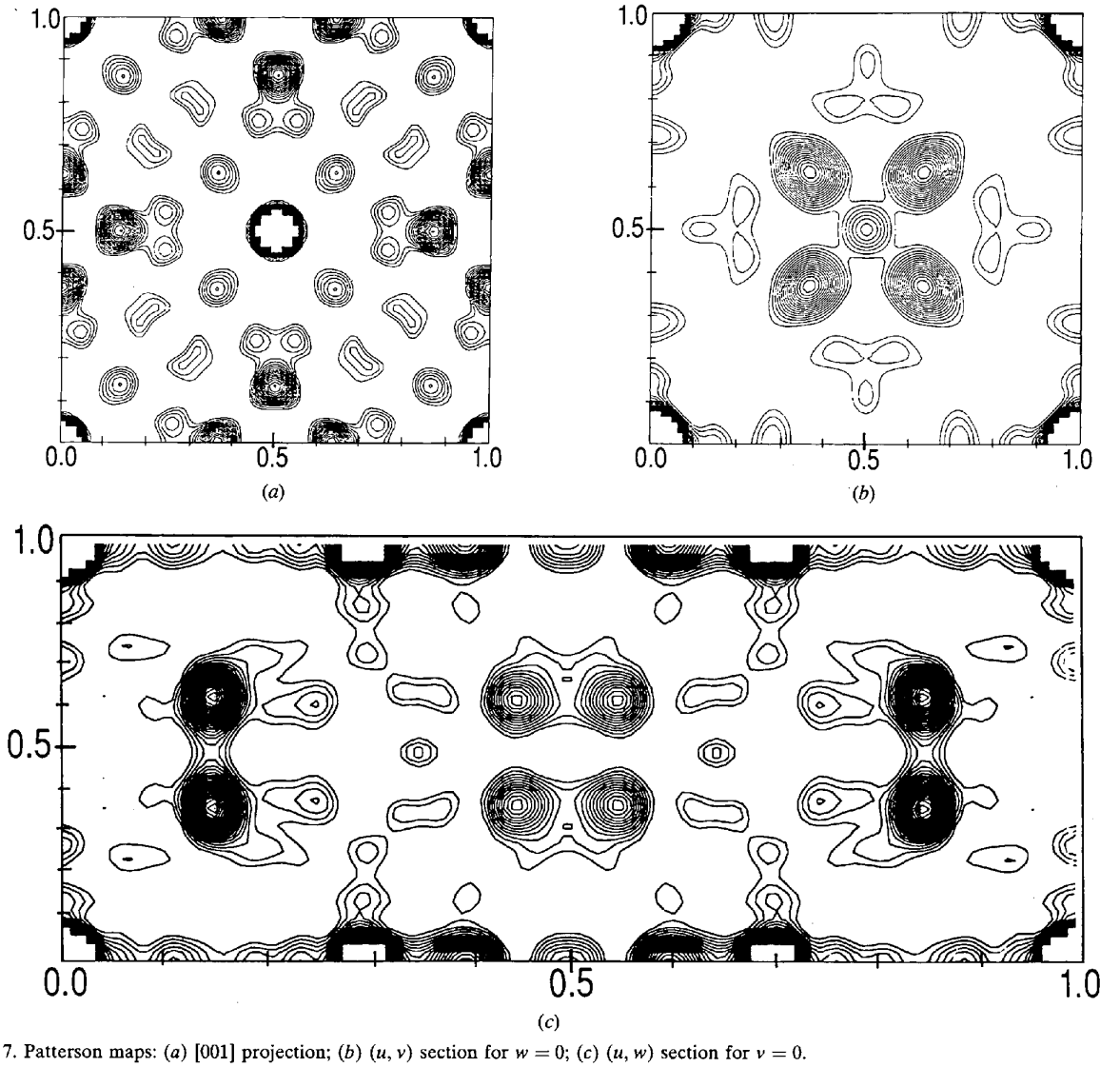

Fig. 7. Patterson maps: (*a*) [001] projection; (*b*) (*u*, *v*) section for $w = 0$; (*c*) (*u*, *w*) section for $v = 0$.

be an inversion axis combined with the diagonal mirror. $I\bar{4}2m$ then remains as the only possibility and was therefore assigned as the space group. We knew from other experience that the three-dimensional mirror symmetry can be difficult to ascertain or disprove by CBED patterns in crystals containing faults, see Rømming *et al.* (1994); it may not be surprising that intensity information had to be invoked in order to arrive at the correct space group.

The strongest Patterson peaks can then be accounted for by three groups of atoms, around the 8(*i*) Wyckoff positions listed in Table 3. If each of these groups were centred about an Fe atom, this would mean 24 Fe atoms in the unit cell, whereas the reported composition of the phase indicates the number of Fe atoms to be 20–21. However, it was decided to attempt to build a structure based on Fe atoms surrounded by Al atoms at two or three of these positions, with $I\bar{4}2m$ as the space group.

4.2. *Fourier syntheses*

From these models, we could calculate structure-factor signs and phases, with the aim of locating the aluminium atoms in Fourier maps. Since the space group is non-centrosymmetric, this Fourier approach based on the present kind of data has its limitations. But the symmetric projections, in particular [001], showed some distinct and stable features. Prominent peaks appeared at the three (x, y) positions marked *A*, *B* and *C* in the [001] projection (Fig. 8*a*). A number of Fourier sections normal to the z axis were calculated in order to locate the aluminium atoms. An example is shown in Fig. 8(*b*) at $z = 0.28$. The peak at a *B*-type projected position (0.45, 0.20, 0.28) together with the symmetry-related position at the height $z = 0.22$ is seen to form a characteristic buckled pentagonal net. Two other *B* positions were found, these indicate a tenfold coordination polyhedron around the Fe atom, as found in other aluminium-rich intermetallic phases with iron or manganese, in particular Al_6Mn/Al_6Fe (Walford, 1965) and β-$Al_{4.5}FeSi$ (Rømming *et al.*, 1994). Chemically reasonable structure models with such polyhedra around Fe atoms at the diagonal mirror, 8(*i*), and joined by edges and corners could then be constructed. Intensity calculations from these models reproduced the strong reflections. However, *R* values calculated for different projections were generally around or above 50% and the question remained whether the 20 Fe atoms could be accommodated statistically on the three 8(*i*) positions listed in Table 3 or by adding a fourfold Fe position at the $\bar{4}$ axis.

4.3. *Direct methods: maximum entropy and likelihood, or the tangent formula*

A different approach to structure solution was attempted using the method of maximum entropy coupled with likelihood evaluation (Bricogne, 1984; Bricogne & Gilmore, 1990) as implemented in the *MICE* computer program (Gilmore *et al.*, 1990). For a review and a detailed description of the method, see Gilmore (1996); for an example of the method in action with three-dimensional electron diffraction data, see Voigt-Martin *et al.* (1994). Both data sets were used and gave very similar results. In both cases, the data were normalized to give unitary structure factors using the *MITHRIL* computer program (Gilmore, 1984) and electron scattering factors. The data were then passed to the *MICE* program. Because the data are subjected to such large errors, a large basis set was chosen comprising 20 reflections chosen as follows:

Table 3. *Possible Fe positions derived from Patterson peaks*

		x	*y*	*z*
Fe1	8(*i*)	0.18	0.18	0.575
Fe2	8(*i*)	0.18	0.18	0.275
Fe3	8(*i*)	0.18	0.18	0.875

(i) A single reflection to define the origin; the enantiomorph was left undefined; it was set *de facto* by the use of phase permutation.

(ii) Five *h*00 reflections with phases derived from energy-filtered CBED measurements.

(iii) 14 reflections were given permuted phases. Nine of these were noncentrosymmetric and given phase permutations of the type $\pm\pi/4$, $\pm 3\pi/4$. The remaining five were centrosymmetric and given phases 0, π.

If a full factorial design was used in permutation, $2^5 \times 4^9 = 8\,388\,608$ phase sets would be generated. Each needs to be subjected to entropy maximization and likelihood evaluation, so that the net calculation is simply not feasible. To reduce the computation, a Golay code was used as a source of phase permuation (Bricogne, 1993, 1997). This yields only 4096 phase sets, among these there will be at least one that has at most three wrong signs. Each of the 4096 phase combinations was subjected to entropy maximization and likelihood evaluation. The likelihoods were analysed using the *t* test (Shankland *et al.*, 1993). The nine top ranked maps were inspected. Peak lists were in general agreement with the models proposed from the Patterson–Fourier attempt. The three peaks at the 8(*i*) positions which had been deduced from the Patterson maps were always the strongest, indicating that the 20–21 Fe atoms should indeed be distributed among these. In addition, there were always three prominent peaks at general 16(*j*) positions of type *B* in the [001] Fourier projection. The positions of 72 atoms (24 Fe/Al + 48 Al) out of approximately 110 atoms in the unit cell appeared to be well established. In addition, peaks always appeared at the $\bar{4}$ axis and at one or two further 8(*i*) positions; the peak list in Table 4 is an average of 12 runs.

Another direct-method procedure based on the tangent formula (Karle & Hauptmann, 1966) produced

Table 4. *Peaks from 12 maximum-entropy peak lists; average positions with standard deviations of peaks listed among the 12 strongest peaks in all lists*

	Position	*x*	*y*	*z*
Fe1	8(*i*)	0.1803 (2)	0.1803 (2)	0.5749 (3)
Fe2/Al	8(*i*)	0.1807 (9)	0.1807 (9)	0.2754 (3)
Fe3/Al	8(*i*)	0.1839 (13)	0.1839 (13)	0.8748 (8)
Al4	16(*j*)	0.325 (3)	0.033 (2)	0.075 (2)
Al5	16(*j*)	0.319 (10)	0.045 (19)	0.373 (2)
Al6	16(*j*)	0.321 (7)	0.040 (7)	0.775 (3)
Al7	4(*e*)	0.000	0.000	0.075 (6)
Al8	8(*i*)	0.189 (3)	0.189 (3)	0.977 (1)
Al9	8(*i*)	0.193 (4)	0.193 (4)	0.172 (2)
Al11	4(*e*)†	0.000	0.000	0.35 (2)
Al12	4(*e*)	0.000	0.000	0.234 (15)

† Only in six of twelve.

essentially the same ten peaks. After generation of Σ_2 triplets and negative quartet invariants, the phases of two reflections, 1,4,17 and 057, were set to −93 and 0°, respectively, to define the origin. Expanding these *via QTAN* (Langs & De Titta, 1975) produced a total of 96 phases with a mean difference of just 20.8° from those phases calculated from the final model. This procedure produced essentially the same ten peaks. From these results, we could then construct a structure model with 110 atoms in the unit cell, based on the Fourier peaks and acceptable interatomic distances. The model (Fig. 9) can be described by ten-coordinated $FeAl_{10}$ polyhedra joined by edges and corners. An eightfold Al position at the Wyckoff position 8(*g*) has been added in order to complete the Al polyhedron around Fe1.

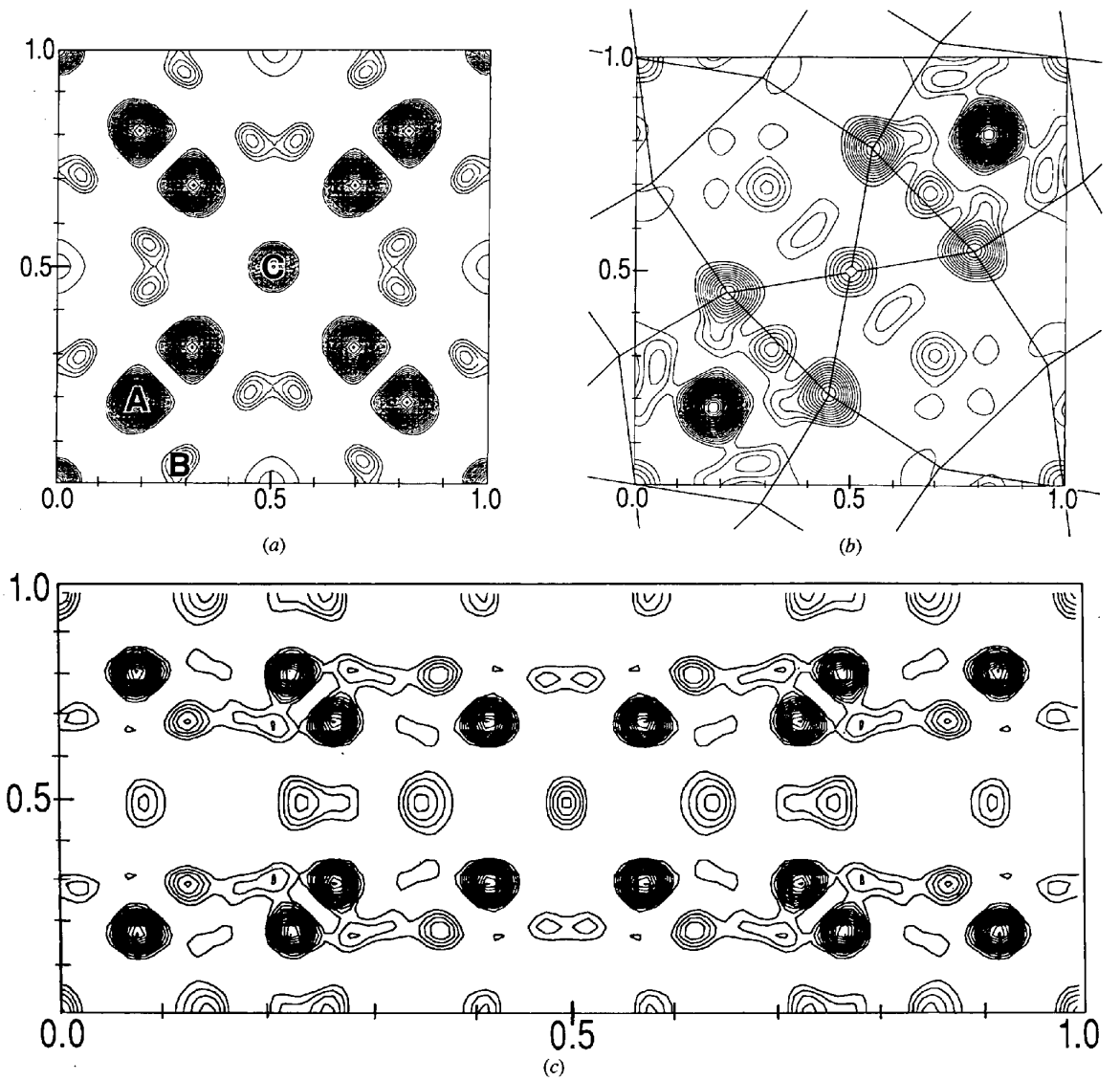

Fig. 8. Fourier maps. (*a*) Early [001] projection based on signs determined mainly from Fe positions; (*b*) (*x*, *y*) section at $z = 0.28$ showing Fe2, and Al6 atoms forming a pentagonal network; (*c*) [010] projection.

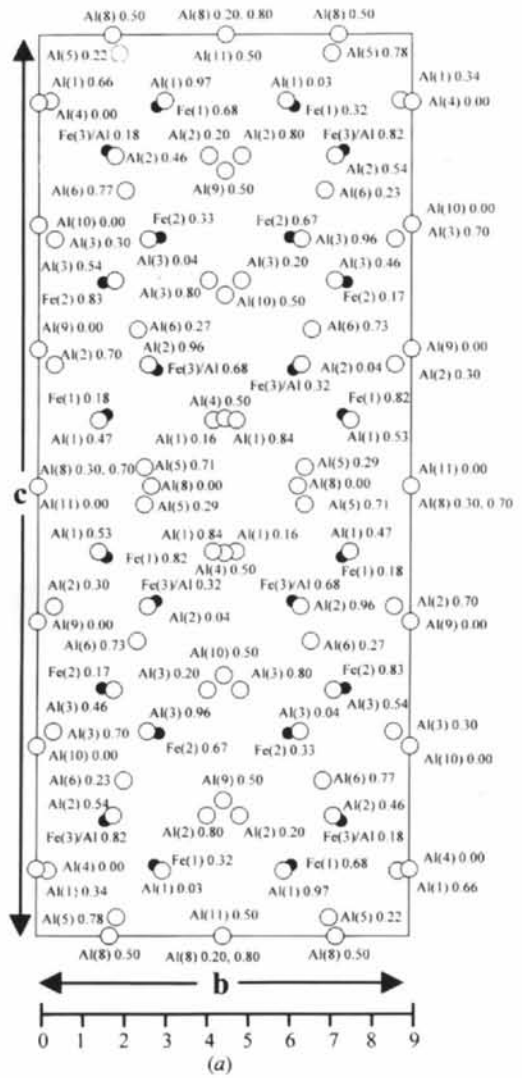

(a)

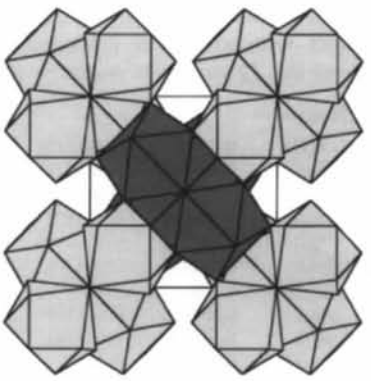

(b)

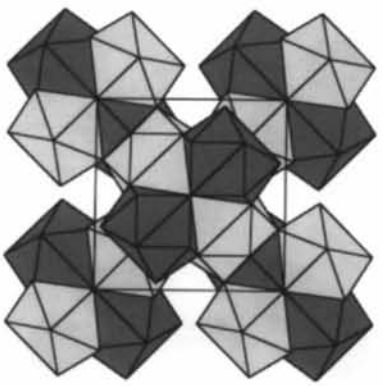

(c)

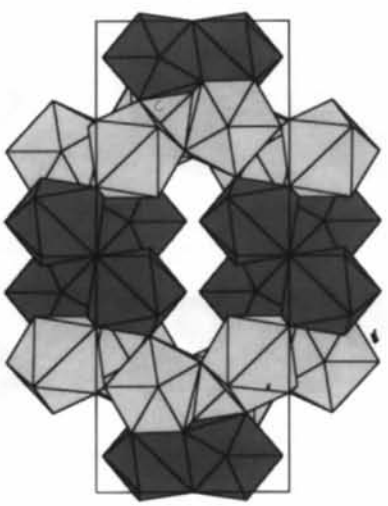

(d)

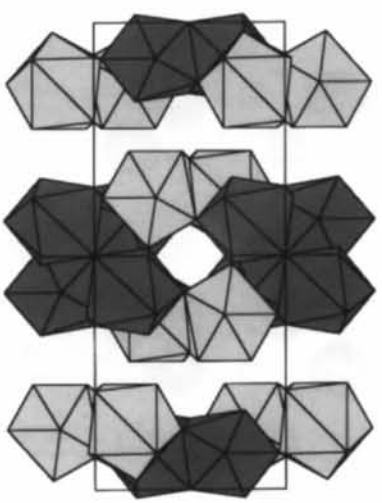

(e)

Fig. 9. Projections of the structure (*a*) seen along the *a* axis with Fe atoms as closed and Al atoms as open circles; (*b*) packing of $FeAl_{10}$ polyhedra around Fe1 (dark) and Fe2 viewed along the *c* axis; (*c*) similarly for Fe1 and Fe3; (*d*) and (*e*) similar views along the *a* axis.

5. Confirmation of the structure. Incorporation of CBED results. Dynamical correction of *hk*0 intensities. Least-squares refinement

For a confirmation of this structure model, consider first the CBED results listed in Table 1. The structure-factor amplitudes and signs obtained for the *h*00 and *hh*0 reciprocal rows agreed well with the structure model, as seen by the projections onto the two rows in Figs. 10(*a*) and (*b*), and by a Fourier projection calculated by a combination of CBED and precession structure factors in Fig. 11(*a*). (The signs for the latter are taken from the structure model.) From these calculations, we concluded that the projected structure must be essentially correct.

As a further check, a dynamical correction procedure for the precession data in *hk*0 has been developed by Gjønnes *et al.* (1998), where details are given. By comparing the precession data with the CBED values for the *h*00 and *hh*0 rows, a value for the thickness was established. An iteration procedure based on the so-called Bethe potentials was then used for determination

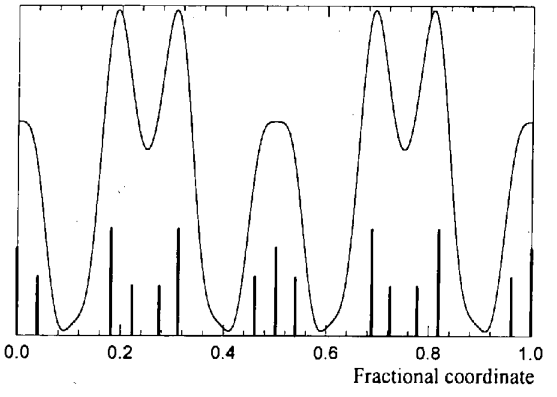

(*a*)

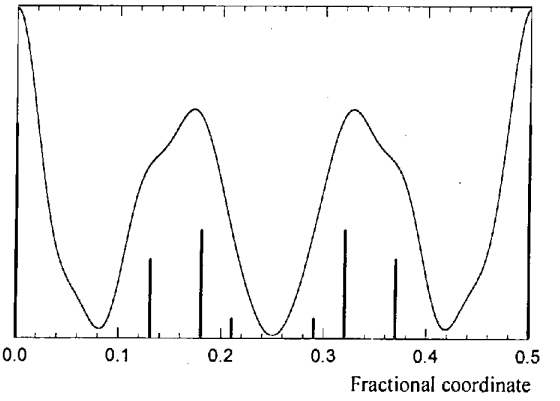

(*b*)

Fig. 10. Fourier projections onto the directions (*a*) [010] and (*b*) [110] calculated from the CBED structure factors. Arbitrary units. The vertical bars indicate projected atom positions from the structure model.

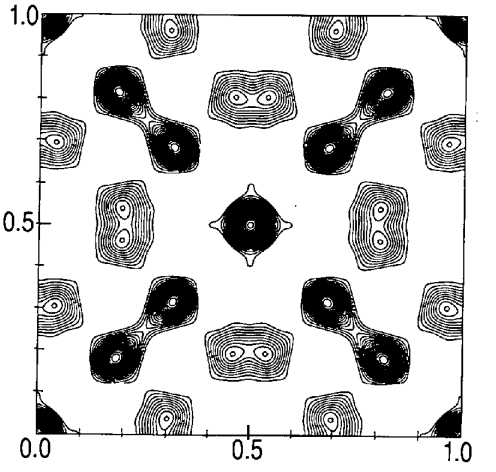

(*a*)

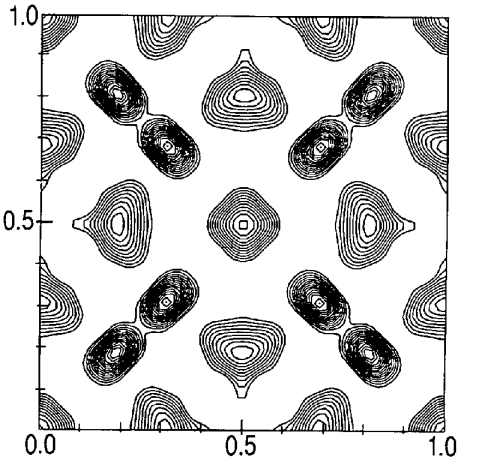

(*b*)

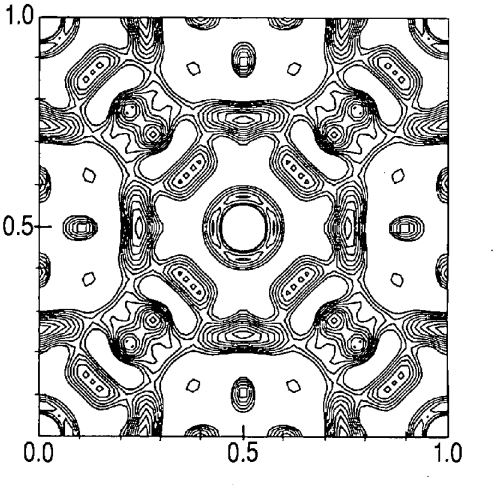

(*c*)

Fig. 11. Fourier projections along [001]. (*a*) Calculated from CBED structure factors plus other U_{hk0} from precession data with signs from model; (*b*) calculated from the dynamically corrected U_{hk0}; (*c*) difference Fourier between (*b*) and 86 projected atoms, *i.e.* without Al8, Al9 and Al10.

Table 5. *Preliminary atom coordinates*

	Position	x	y	z
Fe1	8(*i*)	0.180	0.180	0.575
Fe2/Al	8(*i*)	0.181	0.181	0.275
Fe3/Al	8(*i*)	0.183	0.183	0.875
Al4	16(*j*)	0.325	0.033	0.076
Al5	16(*j*)	0.319	0.045	0.373
Al6	16(*j*)	0.321	0.041	0.775
Al7	4(*e*)	0.000	0.000	0.074
Al8	8(*i*)	0.22	0.22	0.982
Al9	8(*i*)	0.22	0.22	0.168
Al10	8(*g*)	0.500	0.220	0.000
Al11	4(*e*)	0.000	0.000	0.35
Al12	4(*e*)	0.000	0.000	0.21
Al13	2(*b*)	0.000	0.000	0.500

of the Fourier potentials U_{hk0} from the precession intensities and the known U_{h00} and U_{hk0}. This procedure was applied for the four most likely sign combinations, as derived from inequalities. From the corrected potentials thus obtained, a new [001] Fourier projection was calculated (Fig. 11*b*). A difference Fourier map for this projection (Fig. 11*c*) was constructed as the difference between Fig. 11(*b*) and a map that included 86 atoms which were taken to be well located in this projection, *viz* the three Fe and Fe/Al positions [8(*i*)] on the diagonal mirror, three Al in general positions [16(*j*)] and 14 atoms on the axis. Three eightfold Al positions that were considered less certain had thus been left out: two on the diagonal mirror [8(*i*)] and one on the twofold horizontal axis [8(*g*)]. The most prominent features in the (x, y) difference map appeared at a position corresponding to 8(*g*), *i.e.* (0.5, 0.22, 0) and at the 8(*i*) position with $x = y = 0.22$.

The z coordinates for some of the atoms appeared less certain from the maximum-entropy peak lists. These atom positions were adjusted in the z direction so as to give better atomic distances and at the same time somewhat better fit to intensities in [100], [110], [001] and [111] projections. The resulting preliminary coordinates are listed in Table 5; the corresponding interatomic distances were satisfactory. It should also be noted that the corrected *hk*0 structure factors obtained by the correction procedure gave a substantially better fit to this model than had been obtained for the experimental precession data, see Table 6; the R value in *hk*0 was reduced from 0.46 to 0.34, before the adjustment of coordinates, which reduced R further, to 0.30. By using the uncorrected F's, corresponding improvements of about 0.05 were obtained in all major projections.

At this stage, one could conclude with the structure model as a satisfactory result. Based on positions derived from direct methods and Fourier maps, the model produced chemically reasonable coordinations and distances and might be the best that could be obtained by essentially kinematical interpretation of the

Table 6. *Structure factors* $|F_{hk0}|$: F_{calc} *from the structure model;* $F_{obs} = I_{hkl}$ *(precession data) and* F_{corr} *from the correction procedure*

hkl	F_{obs} (precession)	F_{calc} (model)	F_{corr}
110	0.00625	0.00190	0.00290
200	0.01101	0.01160	0.01191
220	0.00813	0.00494	0.00199
310	0.00811	0.00804	0.00662
330	0.01558	0.03325	0.03872
400	0.01058	0.01344	0.01592
420	0.00313	0.00219	0.00132
440	0.00522	0.00570	0.00750
510	0.00253	0.00144	0.00323
530	0.01035	0.00781	0.00580
550	0.01093	0.00655	0.00773
600	0.01301	0.01519	0.01275
620	0.00187	0.00206	0.00149
640	0.00145	0.00266	0.00351
660	0.00813	0.00642	0.00226
710	0.00601	0.00245	0.00209
730	0.00370	0.00450	0.00209
750	0.00142	0.00016	0.00069
770	0.00207	0.00389	0.00158
800	0.00869	0.00794	0.00653
820	0.00779	0.00345	0.00518
840	0.00063	0.00191	0.00310
860	0.00680	0.00344	0.00490
910	0.00085	0.00301	0.00188
930	0.00396	0.00351	0.00297
950	0.00095	0.00131	0.00331
970	0.00066	0.00016	0.00192
10,0,0	0.00214	0.00278	0.00356
10,2,0	0.00226	0.00124	0.00147
10,4,0	0.00115	0.00237	0.00038

Table 7. *Atom coordinates from least-squares refinement*

	x	y	z	U^{11} (Å^2)
Fe1	0.1838 (10)	0.1838 (10)	0.5792 (4)	0.00663
Fe2	0.1740 (13)	0.1740 (13)	0.2750 (6)	0.02008
Fe3/Al	0.183 (2)	0.183 (2)	0.8716 (9)	0.03534
Al1	0.337 (2)	0.031 (2)	0.0729 (6)	0.00948
Al2	0.295 (3)	0.044 (3)	0.3657 (9)	0.02409
Al3	0.295 (2)	0.044 (2)	0.7729 (8)	0.01783
Al4	0.00000	0.000	0.0748 (11)	0.00627
Al5	0.215 (3)	0.215 (3)	0.9793 (14)	0.02891
Al6	0.233 (4)	0.233 (4)	0.173 (2)	0.06220
Al8	0.500	0.197 (4)	0.00000	0.02748
Al9	0.000	0.000	0.3488 (10)	0.00001
Al10	0.000	0.000	0.211 (3)	0.05570
Al11	0.000	0.000	0.50000	0.00001

present intensity data. However, it was decided to try a three-dimensional refinement of the model. The *SHELXL*97 program (Sheldrick, 1997) was applied to the complete set of 598 intensities. A very poor fit to the intensities was obtained, as measured by WR2, which was reduced only from 0.797 to 0.758, with $R1 = 0.42$. The shifts in atom positions from the model (Table 7) were quite small, *viz* less than 0.25 Å; the resulting interatomic distances were indeed reasonable, see Table 8. The refined coordinates are therefore quoted as the final result for a structure with 110 atoms, including

Table 8. *Interatomic distances in Å, < 3.1 Å*

Fe1—Al4 ×2	2.53	Al4—Al4	2.93
Fe1—Al5 ×2	2.53	Al4—Al5	2.73
Fe1—Al8	2.50	Al4—Al5	2.69
Fe1—Al9	2.29	Al4—Al7	2.99
Fe1—Al10 ×2	2.58	Al4—Al8	2.81
Fe1—Al11	2.77	Al4—Al8	2.68
Fe1—Al13	2.86	Al4—Al9	2.96
Fe2—Fe3/Al	2.75	Al4—Al10	2.59
2Fe—Al5 ×2	2.51	Al4—Al10	2.93
Fe2—Al6 ×2	2.43	Al5—Al6	3.09
Fe2—Al6 ×2	2.51	Al5—Al6	2.84
Fe2—Al9	2.31	Al5—Al9	2.88
Fe2—Al11	2.70	Al5—Al11	2.93
Fe2— Al12	2.58	Al6—Al6 ×2	2.66
Fe3/Al—Al4 ×2	2.62	Al6—Al9	2.93
Fe3/Al—Al5 ×2	2.43	Al6—Al9	2.76
Fe3/Al—Al6 ×2	2.65	Al6—Al12	2.66
Fe3/Al—Al7	2.54	Al7—Al8 ×2	2.93
Fe3/Al—Al8	2.36	Al7—Al12	2.94
Fe3/Al—Al12	2.90	Al8—Al10 ×2	2.56
		Al9—Al12	3.02
		Al10—Al13	2.68
		Al11—Al12	2.98

20–21 Fe atoms which are distributed on three eightfold positions as indicated. Attempts to refine occupation numbers failed. This is often a difficult process and becomes very uncertain when dynamical effects are large.

6. Discussion

It may be noted that the structure model presented here implies some disorder through the statistical distribution of Fe/Al on at least one of the Fe positions in the model. There are other indications of disorder or faults as well: Skjerpe (1988) noted extensive faults on (110); in the present study, we observed faults or modulations also on (001), as revealed by the c^* rows in several of the precession patterns reproduced in Fig. 5, especially Fig. 5(*c*). These features should be borne in mind in a discussion of the structure and model and its accuracy. We have formulated the above Al_mFe structure model as a network of Al_{10} polyhedra around the Fe positions that were first deduced from Patterson maps and then established by the direct-method maximum-entropy calculations. The polyhedra share edges and corners, like the similar polyhedra in Al_6Fe (Walford, 1965). Tenfold coordination of Al around Fe is found also in $Al_{13}Fe_4$ (Black, 1955), β-$Al_{4.5}FeSi$ (Rømming *et al.*, 1994) and in the hexagonal α-AlFeSi (Corby & Black, 1977). A different representation of the structure is shown in Fig. 12: by two different double layers normal to the *c* axis, *viz* a layer (I) at levels $z = 0$ and $z = 0.075$ and another (II) at $z = 0.150$ and 0.225. The layers repeat at 0.275 and 0.350 (II) and at 0.425 and 0.50 (I) *etc.* and are seen to form a distorted CsCl/b.c.c.-type network with 20 Fe and 90 Al atoms and 16 vacancies. From this description, the Al_mFe structure can be regarded as intermediate between the CsCl-type arrangement of iron and aluminium found around the FeAl composition and the tenfold coordination around Fe in the stable intermetallic phases in the Al-rich end of the Al–Fe system, in particular the nearly stable Al_6Fe. The role of vacancies in forming the tenfold coordination polyhedra from a CsCl-type cube is illustrated in Fig. 13. By adding Al on two of the cube faces or by removing an atom from one cube corner and

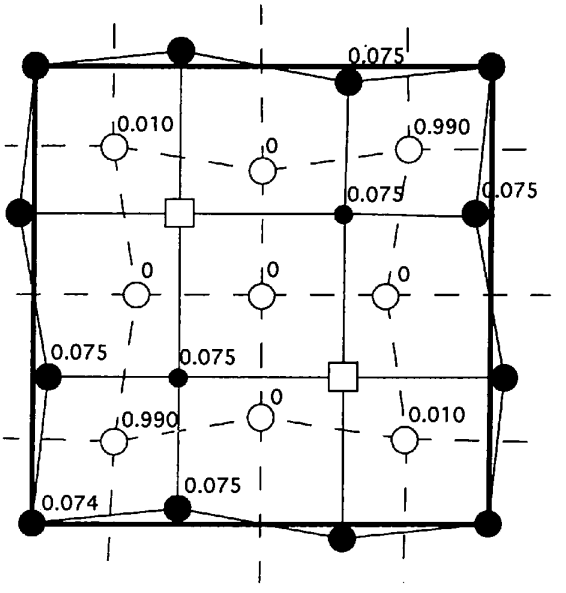

(*a*)

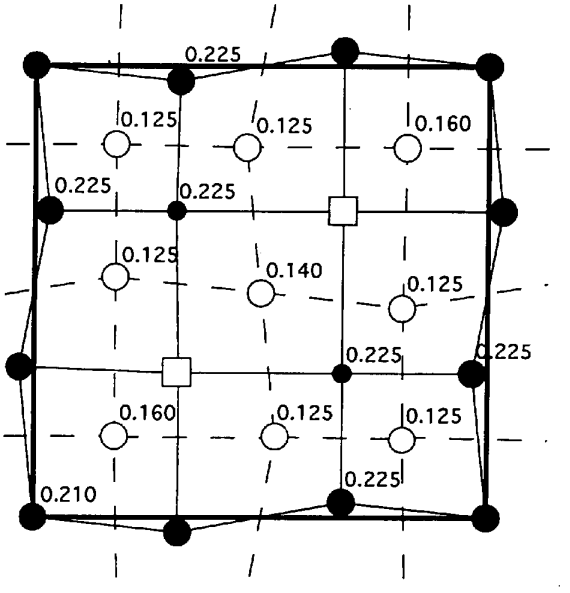

(*b*)

Fig. 12. Two double distorted CsCl/b.c.c. layers (*a*) around $z = 0$ (open symbols) and $z = 0.075$ (filled symbols), and (*b*) around $z = 0.15$ (open) and $z = 0.225$ (filled). Fe are small, Al large, squares vacant.

adding Al on three faces, one obtains the Fe1 and Fe2 polyhedra in the present model by only slight distortions of the polyhedron. By removing two Al atoms from a cube edge and adding Al atoms on four faces, one obtains a further polyhedron which is close to Al_6Mn. It should be mentioned that Skjerpe (1988) suggested a CsCl-like arrangement around iron in his study of the phase. Fig. 13 may suggest that the two 8(*i*) Al positions, 8 and 9, could be replaced by indicated 'vacancy' positions. This would lead to the same types of coordination polyhedra around Fe but interchanged between the different Fe positions. We have no direct evidence of this particular kind of disorder, which could be connected with the modulations along the *c* axis and/or the Fe/Al disorder. From such considerations, one should regard the present structure as an average structure, which may contain statistical elements in addition to the Fe/Al occupation indicated in Table 6.

It should be apparent from the present study that a structure model for Al_mFe could only be derived from three-dimensional intensity information and that such information can be collected by electron diffraction even from crystal specimens of irregular shape and moderate thickness. The precession technique by Vincent & Midgley (1994) was found to be a substantial improvement over selected-area spot patterns by reducing the effects of dynamical scattering on the intensity data. Although appreciable dynamical effects remained, a structure solution could be obtained on the basis of kinematical scattering calculations and procedures taken from X-ray crystallography. An important conclusion seems to be that the phases derived by the direct-method procedures are quite robust against dynamical scattering effects. The reason behind this and other sucessful structure determinations based on kinematical interpretation of intensities (see *e.g.* Zou, 1995) may be that the kind of statistical relations that form the basis for direct methods in crystallography are to some extent preserved also under the condition of dynamical scattering. Some recent theoretical studies (Tivol, 1995; Peng & Wang, 1994) point in this direction, as does the channelling argument presented by Van Dyck & Op de Beeck (1996). The comparison with the CBED results of Cheng *et al.* (1996) and the dynamical corrections applied here lends further support to this conclusion.

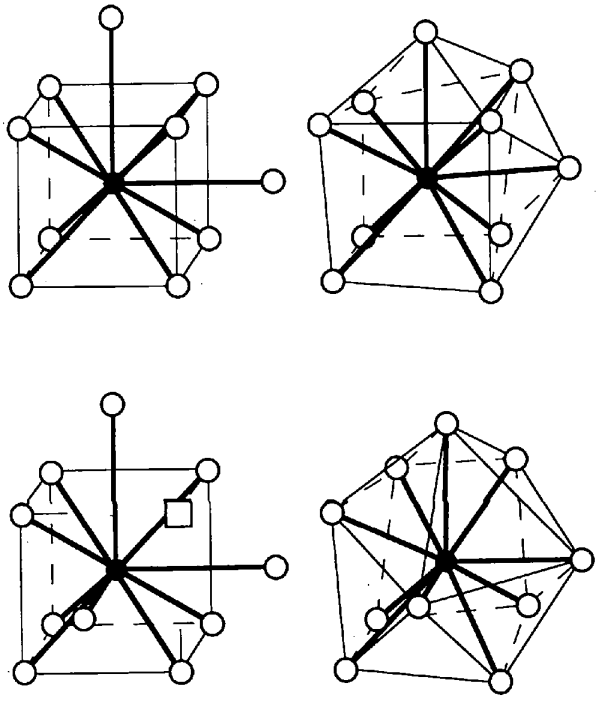

Fig. 13. Coordination polyhedra around Fe1 (top) and Fe2 (bottom) shown to the right can be formed from the CsCl-type units shown to the left. Fe atoms are shown as filled circles, Al atoms as open circles. The squares are vacancies referred to CsCl.

Refinement is a different matter. Sucessful two-dimensional refinements based on electron diffraction data collected from thin crystals in projection have been shown by Weirich *et al.* (1996), assuming kinematical scattering and by Zandbergen *et al.* (1995) using dynamical scattering calculations. The present structure needed three-dimensional refinement from data that were obtained by integrations, from crystal that are quite thick, *ca* 1000 Å. The dynamical corrections derived for the *hk*0 reflections were appreciable. This is seen as the main reason for the poor fit to intensities that was obtained in the present refinement. The very reasonable result in terms of coordinates and distances may be associated with the fact that the precession intensities were collected by integrations through many different diffraction conditions. Ideally, structure refinement should include some kind of dynamical calculation also for data collected in the present kind of experiment. The development of procedures for this sort of dynamical refinement remains an important task, together with the improvement in the experimental procedures that are now possible, *e.g.* by means of energy filtering and better detection media, *e.g.* imaging plates or slow-scan CCD cameras. When these improvements are introduced, and procedures for combination with CBED-based profile measurements are developed further, it seems to us that structure determination based on quantitative electron diffraction/high-resolution electron microscopy will have a wide field of application, even in cases where three-dimensional data are required and crystals are not very thin.

YFC is grateful to the Alexander von Humboldt Foundation for a Fellowship. Financial support from the Norwegian Research Council is acknowledged; thanks are also due to P. A. Midgley and Bristol University for the use of their precession equipment and to Dr A. Holt

for the use of his program *Crystal Designer*. CJG thanks the EPSRC for support. DLD acknowledges support from NSF grant CHE94-17835.

References

Andersen, S. J., Zandbergen, H. W., Jansen, J., Træholt, C., Tundal, U. & Reiso, O. (1998). *Acta Mater.* In the press.

Berg, B. S., Hansen, V., Midgley, P. A. & Gjønnes, J. (1998). In preparation.

Bird, D. M. & Saunders, M. (1992). *Acta Cryst.* A**48**, 555–562.

Black, P. J. (1955). *Acta Cryst.* **8**, 175–182.

Bricogne, G. (1984). *Acta Cryst.* A**40**, 410–445.

Bricogne, G. (1993). *Acta Cryst.* D**49**, 37–60.

Bricogne, G. (1997). *Methods Enzymol.* **276**, 424–448.

Bricogne, G. & Gilmore, C. J. (1990). *Acta Cryst.* A**46**, 284–297.

Buerger, M. J. (1964). *The Precession Method in X-ray Crystallography*. New York: Wiley.

Cheng, Y. F., Nüchter, W., Mayer, J., Weickenmeier, A. & Gjønnes, J. (1996). *Acta Cryst.* A**52**, 923–936.

Corby, R. N. & Black, P. J. (1977) *Acta Cryst.* B**33**, 3468–3475.

Dorset, D. L. (1995). *Acta Cryst.* A**51**, 869–879.

Gilmore, C. J. (1984). *J. Appl. Cryst.* **17**, 42–46.

Gilmore, C. J. (1996). *Acta Cryst.* A**52**, 561–589.

Gilmore, C. J., Bricogne, G. & Bannister, C. (1990) *Acta Cryst.* A**46**, 297–308.

Gjønnes, K. (1997). *Ultramicroscopy*, **69**, 1–11.

Gjønnes, K. & Bøe, N. (1994). *Micron Microsc. Acta*, **25**, 29–44.

Gjønnes, K., Cheng, Y. F., Berg, B. S. & Hansen, V. (1998). *Acta Cryst.* A**54**, 102–119.

Karle, J. & Hauptmann, H. (1966). *Acta Cryst.* **9**, 635–651.

Langs, D. A. & De Titta, G. T. (1975). *Acta Cryst.* A**31**, S16.

Miki, I., Kosuge, H. & Nagahama, K. (1975). *J. Jpn. Inst. Met.* **25**, 1–9.

Peng, L.-M. & Wang, S. Q. (1994). *Acta Cryst.* A**50**, 759–771.

Press, W. H., Flannery, S. A., Teukolsky, S. A. & Vetterling, W. T. (1986). *Numerical Recipes.* Cambridge University Press.

Rømming, C., Hansen, V. & Gjønnes, J. (1994). *Acta Cryst.* B**50**, 307–312.

Shankland, K., Gilmore, C. J., Bricogne, G. & Hashizume, H. (1993). *Acta Cryst.* A**49**, 493–501.

Sheldrick, G. M. (1997). *SHELXL97. Program for the Refinement of Crystal Structures.* University of Göttingen, Germany.

Simensen, C. J., Fartum, P. & Andersen, A. (1984). *Fresenius Z. Anal. Chem.* **319**, 286–292.

Skjerpe, P. (1988). *Acta Cryst.* B**44**, 480–486.

Skjerpe, P., Gjønnes, J. & Langsrud, Y. (1987). *Ultramicroscopy*, **22**, 239–250.

Spence, J. C. H. (1993). *Acta Cryst.* A**49**, 231–260.

Taftø, J. & Metzger, T. H. (1985). *J. Appl. Cryst.* **18**, 110–113.

Tivol, W. F. (1995). *Acta Cryst.* A**51**, 708–716.

Tsuda, K. & Tanaka, M. (1995). *Acta Cryst.* A**51**, 7–19.

Van Dyck, D. & Op de Beeck, M. (1996). *Ultramicroscopy*, **64**, 99–107.

Vincent, R., Bird, D. M. & Steeds, J. W. (1984). *Philos. Mag.* A**50**, 745–763.

Vincent, R. & Midgley, P. A. (1994). *Ultramicroscopy*, **53**, 271–282.

Voigt-Martin, I. C., Yan, D. H., Gilmore, C. J., Shankland, K. & Bricogne, G. (1994). *Ultramicroscopy*, **56**, 271–288.

Walford, L. K. (1965). *Acta Cryst.* **18**, 287–291.

Weirich, T. E., Ramlau, R., Simon, A., Hovmöller, S. & Zou, X. D. (1996). *Nature (London)*, **382**, 144–146.

Westengen, H. (1982). *Z. Metallkd.* **73**, 360–368.

Zandbergen, H. W., Van Zwett, E. J., Jansen, J., Sarrao, J. L., Maple, M. B., Fisk, Z. & Cava, R. J. (1995). *Philos. Mag. Lett.* **71**, 131–138.

Zou, X. D. (1995). *Electron Crystallography of Inorganic Structures.* Stockholm University, Stockholm, Sweden.

Zou, X. D., Hovmöller, S., Parras, M., Gonzales-Calbet, J. M., Valet-Regi, M. & Grenier, J. C. (1993). *Acta Cryst.* A**49**, 27–35.